Nanoscale

PAPER

View Article Online
View Journal | View Issue

Cite this: *Nanoscale*, 2017, **9**, 14248

Nanotopography mediated osteogenic differentiation of human dental pulp derived stem cells†

Akash Bachhuka, ‡[a,b] Bahman Delalat, ‡[a] Soraya Rasi Ghaemi, [a] Stan Gronthos, [c] Nicolas H. Voelcker *[a,d,e,f,g] and Krasimir Vasilev *[a,h]

Advanced medical devices, treatments and therapies demand an understanding of the role of interfacial properties on the cellular response. This is particularly important in the emerging fields of cell therapies and tissue regeneration. In this study, we evaluate the role of surface nanotopography on the fate of human dental pulp derived stem cells (hDPSC). These stem cells have attracted interest because of their capacity to differentiate to a range of useful lineages but are relatively easy to isolate. We generated and utilized density gradients of gold nanoparticles which allowed us to examine, on a single substrate, the influence of nano-feature density and size on stem cell behavior. We found that hDPSC adhered in greater numbers and proliferated faster on the sections of the gradients with higher density of nanotopography features. Furthermore, greater surface nanotopography density directed the differentiation of hDPSC to osteogenic lineages. This study demonstrates that carefully tuned surface nanotopography can be used to manipulate and guide the proliferation and differentiation of these cells. The outcomes of this study can be important in the rational design of culture substrates and vehicles for cell therapies, tissue engineering constructs and the next generation of biomedical devices where control over the growth of different tissues is required.

Received 3rd May 2017,
Accepted 7th September 2017

DOI: 10.1039/c7nr03131a

rsc.li/nanoscale

Introduction

Understanding the interactions of biological matter with interphases is of paramount importance for creating advanced medical treatments, diagnostics and therapies.[1–4] The integration and function of medical devices ranging from heart valves to dental implants is dependent on the response of tissue to material surface.[5–8] The precision of many medical diagnostic technologies requires adequate response to biological fluids. The field of cell therapies, which is considered by many as the future of medical treatments, can be realized only if we have the capacity to control cell proliferation, differentiation and expansion on synthetic materials, and provide vehicles for the delivery of these cell.[9–11] Thus, it is not surprising that substantial research efforts have focussed on unravelling the processes and phenomena occurring between cells and material surfaces.

Recently, dental pulp derived stem cells (DPSC) have attracted interest as potent source of autologous cells in a number of area of regenerative medicine, including cell therapies.[12–14] These cells have mesenchymal character and similar to bone marrow stromal cells (BMSC) have the capacity to differentiate into a wide range of other cells.[14,15] It was also shown that DPSC can be a source of induced pluripotent stem (IPS) cells.[16,17] In addition to tooth regeneration and bone reconstruction, other areas such as neuroregeneration,[18] angiogenesis[19] and vasculogenesis, and endocrinology[20] can benefit from DPSC. The attractive sides of these cells is their relative ease of isolation from the pulp of discarded or removed teeth.[14] It was also shown that DPSC can be cultured

[a]*Future Industries Institute, University of South Australia, Mawson Lakes, Adelaide, SA, 5095, Australia. E-mail: krasimir.vasilev@unisa.edu.au; Fax: +(61)8 8302 5689; Tel: +(61)8 8302 5697*
[b]*ARC Centre of Excellence for Nanoscale Bio Photonics, Institute for Photonics and Advanced Sensing, School of Physical Sciences, The University of Adelaide, Adelaide, SA, 5005, Australia*
[c]*Adelaide Medical School, Faculty of Health and Medical Sciences, University of Adelaide, Adelaide, 5005 SA, Australia*
[d]*Melbourne Centre for Nanofabrication, Victorian Node of the Australian National Fabrication Facility, 151 Wellington Road, Clayton, Victoria, 3168, Australia. E-mail: nicolas.voelcker@monash.edu; Tel: +(61)3 9903 9320*
[e]*Drug Delivery, Disposition and Dynamics, Monash Institute of Pharmaceutical Sciences, Monash University, 381 Royal Parade, Parkville, Victoria, 3052, Australia*
[f]*Commonwealth Scientific and Industrial Research Organisation (CSIRO), Clayton, Victoria, 3168, Australia*
[g]*INM-Leibniz Institute for New Materials, Campus D2 2, Saarbrücken, 66123, Germany*
[h]*School of Engineering, University of South Australia, Adelaide, SA 5000, Australia*
†Electronic supplementary information (ESI) available: Supplementary figures showing XPS characterization of surfaces and Fluorescence images of cell differentiation. See DOI: 10.1039/c7nr03131a
‡Equal contribution.

for periods as long as 6 months without changes in morphology or the expression of stem cell markers.[21] These studies demonstrate that DPSC can be maintained and expanded to high numbers, which is a prerequisite for cell therapies and other regenerative medicine applications.

For DPSC and other stem cells to become accessible medical therapies, it is essential to acquire the capacity to control cell differentiation and expansion in an efficient and cost effective manner.[22,23] Current strategies to control stem cell differentiation is *via* soluble factors and chemical formulations.[24,25] However, this approach is rather expensive. Furthermore, some of the soluble factors are of animal origin and can cause regulatory problems because of the danger of transmission of diseases. Emerging cost effective and efficient strategies involve the targeted modification of the culture substrate or deliver vehicle *via* tuning the surface chemistry, ligand type and density, stiffness or topography.[26–30] In this context, surface nanotopography has attracted particular attention since it may provide a tool to mimic the physical microenvironment where cells naturally reside.[31,32]

Surface nanotopography has been extensively investigated and documented to affect the behaviour of a range of cells including dermal,[33] inflammatory,[34] tumor[35] and stem cells.[29,36–43] There are a number of phenomena that takes place when cells interact with nanotopography. When a material is placed into a biological fluid, proteins adhere to its surface within minutes. The amount and conformation of adhered proteins can have a significant influence on the subsequent cell attachment, proliferation, and differentiation.[44,45] In the presence of nanotopography, surface area is generally significantly increased (relative to a smooth surface) which may result in adsorption of greater amount of protein. Another important role that surface topographical features may play is altering the conformation of absorbed proteins. Recent work carried out in solution have demonstrated that the conformation of fibrinogen can be dramatically altered by the curvature of nanoparticles.[46,47] The consequence of fibrinogen unfolding was exposing protein sequences that are shielded in the protein natural conformation. Although this work was carried out in solution, it is reasonable to assume that topographical surface feature at the nanoscale may lead to the same consequence. On the other hand, mechanotransduction due to nanotopography exerts forces on cells which can alter biochemical signalling and induce adaptive functional changes.[48] Furthermore, nanotopography is reported to alter focal adhesion, integrin clustering and cytoskeletal organization of cultured cells.[49,50]

In this study, we explore for the first time the role of controlled nanotopography and tailored outermost surface chemistry on the attachment, proliferation and differentiation of hDPSC. The hypothesis underpinning this work was that carefully designed surface nanotopography can be used to control the behavior of hDPSC. This hypothesis was substantiated by the similarity of hDPSC to MSC, which have been demonstrated to be strongly influenced by surface topography.[29,51] To elucidate the role of nanotopographical features in terms of height and lateral spacing, we generated nanoparticle density gradients *via* a method which we reported earlier.[52,53] To create surface topography at the nanoscale we used nearly monodispersed gold nanoparticles (AuNP) of diameters of 16, 38 or 68 nm. The benefit of using gradients is that studies can be conducted using minimum number of substrates thus avoiding errors associated with the use of multiple uniformly modified samples. In addition, the gradient format speeds up analysis, reduces the number of cells used in the experiments and decreases the experimental variability by directly comparing the data obtained using the same cell population. An issue inherent of many published studies, where nanotopography was used to examine various phenomena, is heterogeneous surface chemistry. We tackled this problem by tailoring the outermost surface chemistry by depositing a 5 nm thin plasma polymer coating on top of the nanoparticles from allylamine vapor. hDPSC were cultured on these model surfaces for periods of up to three weeks and analyzed for proliferation and osteogenic differentiation.

Results and discussion

In order to generate gradients of AuNP, 13 mm round coverslips were first coated with a 20 nm thin layer of plasma polymerized allylamine (AApp). These films carry a population of amine groups which protonate in aqueous medium below pH = 8 and produce a positive surface charge.[54,55] The modified coverslips were then immersed in a rate controlled fashion in a solution of AuNP of three different sizes (16, 38 or 68 nm) using a dip coating method as we have previously reported.[56] Using this technique, we were successfully able to control the time of contact of each region of the AApp coated surface and the gold nanoparticle solution, which resulted in nanoparticle density gradients across the surface. In addition of controlled spacing between nanoscale features, the predetermined size of the immobilized nanoparticles *i.e.* 16, 38 or 68 nm also allowed us to generate surface nanotopography of controlled height. However, these substrates present not only variation in nanotopography but also have mixed chemistry. The underlying AApp coating is amine/nitrogen rich while gold nanoparticles carry carboxyl acid surface groups. We were able to uniquely tailor the outermost surface chemistry by overcoating the nanoparticle density gradients with a 5 nm thin layer of AApp. We have demonstrated in several published studies that AApp films of this thickness are continuous and pinhole free and thus provide uniform surface chemistry across the surface.[57]

These surface overcoatings also change surface energy further leading to the change in surface wettability.[53,58] Using this approach, the stem cells were presented only with changes in nanotopography. Fig. 1a shows AFM images on six equally spaced regions across the nanoparticles density gradients having nanoparticle size of 16 nm (top), 38 nm (middle) and 68 nm (bottom). The nanoparticles were randomly distributed with an increase in nanoparticle density from region 3 mm to

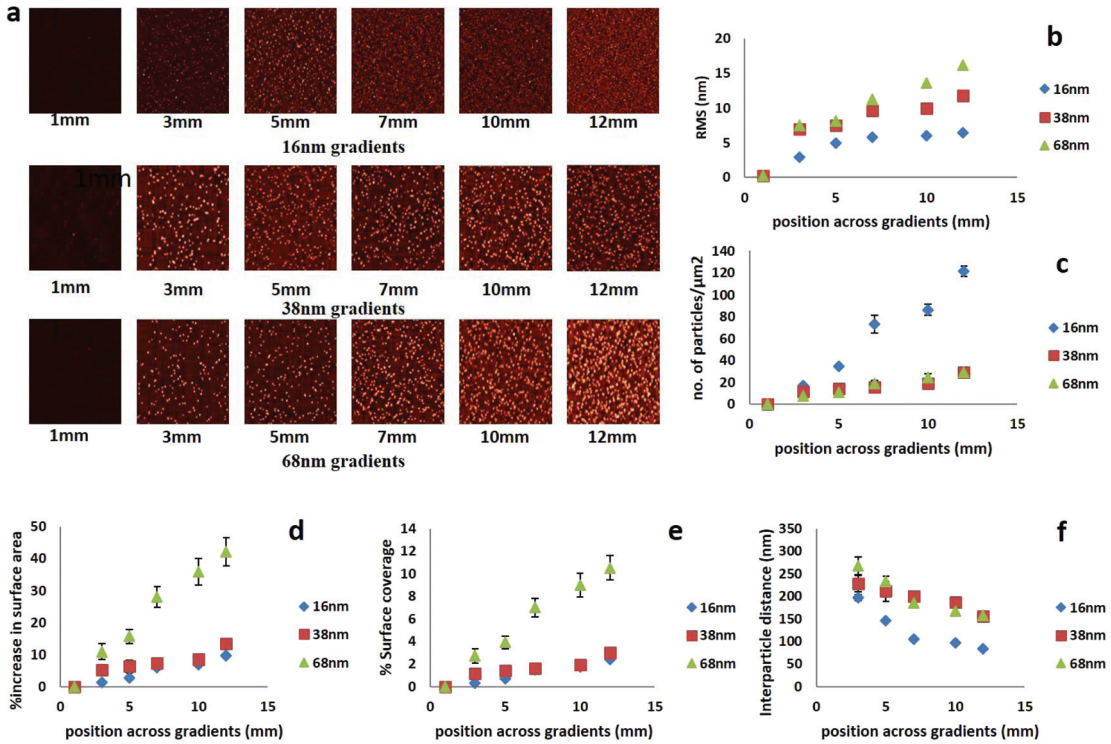

Fig. 1 (a) AFM images of 16, 38 and 68 nm AuNP immobilized on different regions along the gradient samples after overcoating with a 5 nm thin AApp films. Analysis of the AFM images shown in terms of (b) root mean square roughness (RMS), (c) number of particles per μm^2, (d) % increase in surface area, (e) % surface coverage, and (f) interparticle distance. The scan size for all AFM images was 5 μm × 5 μm while all images were scaled relative to the maximum height for like-sized AuNP immobilized surfaces.

region 12 mm and did not form aggregates. The root mean square roughness (RMS) increased with the greater nanoparticle size and density (shown in Fig. 1b). The AFM images were further analyzed to calculate number of particles per μm^2, % increase in surface area, % surface coverage and interparticle distance at different regions of the surface. The number of surface bound nanoparticles per μm^2 increased from 17 ± 2 at region 3 mm to 121 ± 5 at 12 mm in the case of 16 nm AuNP. For nanoparticles of 38 nm diameter, the number of particles increased from 12 ± 3 to 30 ± 3 across the gradient and for 68 nm nanoparticles from 8 ± 2 to 30 ± 3 (Fig. 1c). The increasing number of nanoparticles across the surface resulted in greater surface area and surface coverage as shown in Fig. 1d and e, respectively. The interparticle distance decreased with the increase in density across the gradients for all nanoparticles. The interparticle distance decreased from 196 nm to 83 nm for the 16 nm AuNP, from 228 nm to 155 nm for the 38 nm nanoparticles and from 268 nm to 156 nm for the 68 nm AuNP (Fig. 1f).

XPS was used to analyze the elemental chemical composition across the gradients of nanoparticle density. The survey spectra on 6 regions along the coverslip modified with 16 nm AuNP is shown in Fig. 2a. The data showing the elemental composition of the corresponding spectra for nanoparticle density gradients of 38 and 68 nm are presented in the ESI Fig. S1 and S2.† The atomic percentage of chemical elements on different regions across the gradient are presented in Table S1 of the ESI.†

Fig. 2a shows the increase in the intensity of the Au 4f peak towards region 12 mm which corresponds in increasing number of surface bound nanoparticles. The nitrogen N 1s peak was detected due to the initial underlying layer of allylamine, which aids in electrostatic immobilization of different sized gold nanoparticles. The surface also contained some amount of oxygen which was due to the carboxyl functionalities on the surface of the nanoparticles and some partial oxidation of the surface typical for this type of plasma polymers.[55,57] Survey spectra of nanoparticle density gradient after overcoating with a 5 nm thin layer of plasma polymerized allylamine (AApp) are shown in Fig. 2b. The intensity of the nitrogen N 1s peak increased while gold atomic concentration decreased (Table S1†). However, gold signal was still detectable as XPS sampling depth of *ca.* 10 nm, which is greater than the thickness of the AApp overcoating. A detailed information of the chemical composition across the nanotopography gradients of different sizes, is shown in ESI Table S1.†

To demonstrate the effect of surface nanotopography on cell attachment, hDPSC were cultured on the gradients of different nanotopography scale and AApp control for 12 h.

Fig. 3 shows the fluorescence microscopy images of cells attached on different regions across the gradients. Nuclei (blue) staining was used to quantify the number of attached

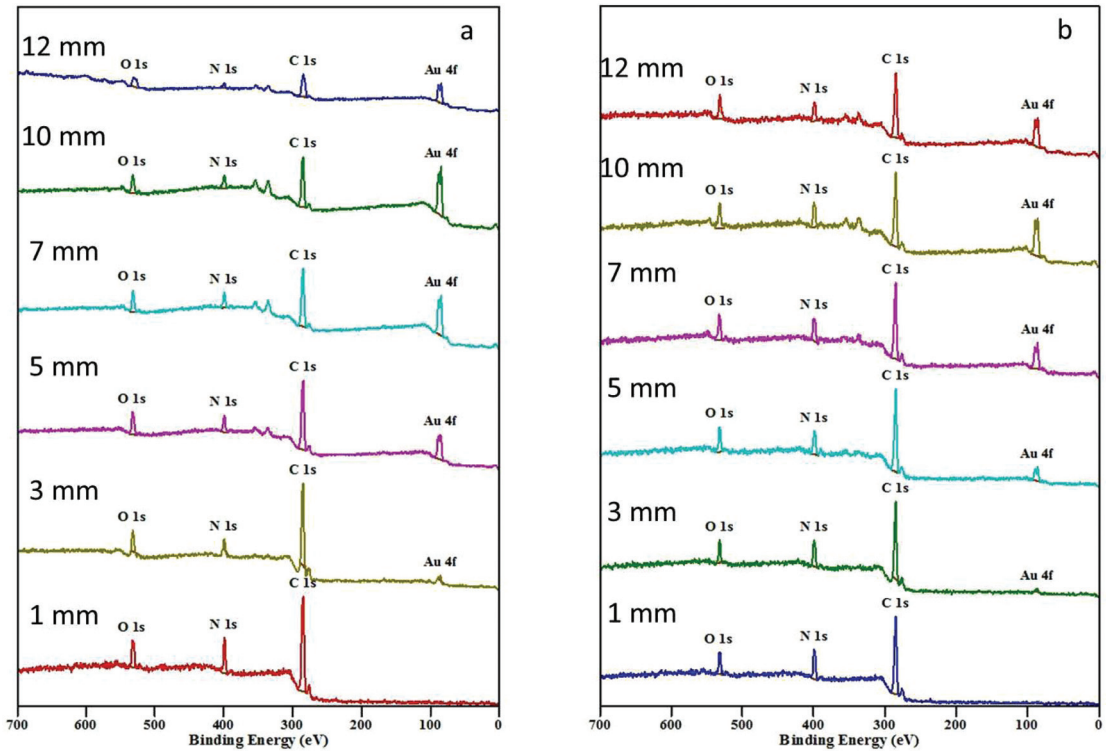

Fig. 2 XPS survey spectra showing the surface chemical composition of a glass coverslip modified with the gradient of 16 nm AuNP (regions 1 mm to 12 mm) before (a) and after deposition of a 5 nm thin overcoating of AApp (b).

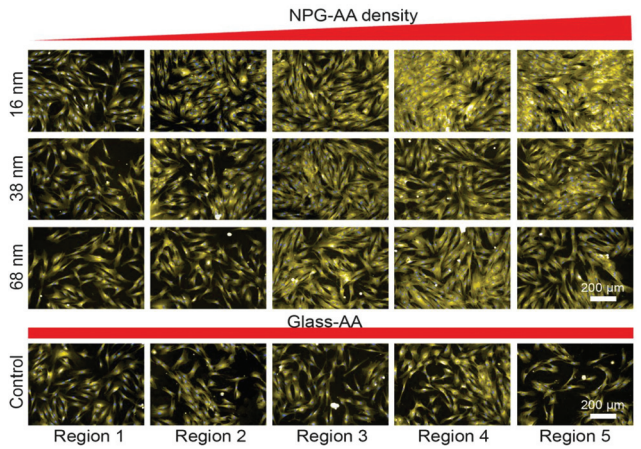

Fig. 3 Laser scanning fluorescence microscopy images depicting cell attachment after 12 h in culture across the gradients of 16 nm, 38 nm, 68 nm nanotopography and smooth AApp control. Regions 1 to 5 correspond to region 1 mm, 3 mm, 6 mm, 9 mm and 12 mm. Magnification of (20×, wide lens) was employed to capture the images.

cells. The images clearly show an increase in the number of adherent cells toward the greater nanoparticle density (region 1 to region 5). In addition, there were greater number of attached cells on the nanotopography gradients compared to a control coverslip coated with the smooth AApp coating only. The data suggest that nanotopography enhances cell adhesion compared to a smooth surface with the same chemistry.

Fig. 4 shows quantitative analysis of cell numbers on smooth AApp surface and across gradients of nanotopography (16, 38 and 68 nm). There was no significant difference in cell number across the control coverslip coated with AApp only (Fig. 4a). In the case of 16 nm nanotopography, cell number per mm^2 significantly increased on regions 4 ($p < 0.01$) and 5 ($p < 0.0001$) compared to region 1 (Fig. 4b). This shows that smaller nanotopography with an interparticle distance of 97 nm or less plays an important role in cell adhesion. When nanotopography was 38 nm, cell number per mm^2 significantly increased on regions 3, 4 and 5 ($p < 0.01$) compared to region 1 (Fig. 4c), suggesting that features of 38 nm high and interparticle distance below 200 nm is favorable for cell attachment. On gradients of 68 nm nanoparticles, cell number was greatest on regions 3 ($p < 0.01$) and 4 ($p < 0.001$) having interparticle distance between 185 and 167 nm, respectively (Fig. 4d). There was no significant difference in cell numbers on regions 2 and 5 compared to region 1. Further increase in nanoparticle density had no effect on the number of adhered cells. The data indicate that both height and spacing between the nanoparticles are strong arbiters for cell adhesion. This is clearly evident in Fig. 4e where the data of the three different nanotopography scales is collectively presented, further suggesting the smaller scale of nanotopography may preferentially encourage cell attachment.

Fig. 5 shows fluorescence microscopy images of cell proliferation on uniformly coated AApp coverslip and across the nanotopography gradients. It can be clearly seen that cell pro-

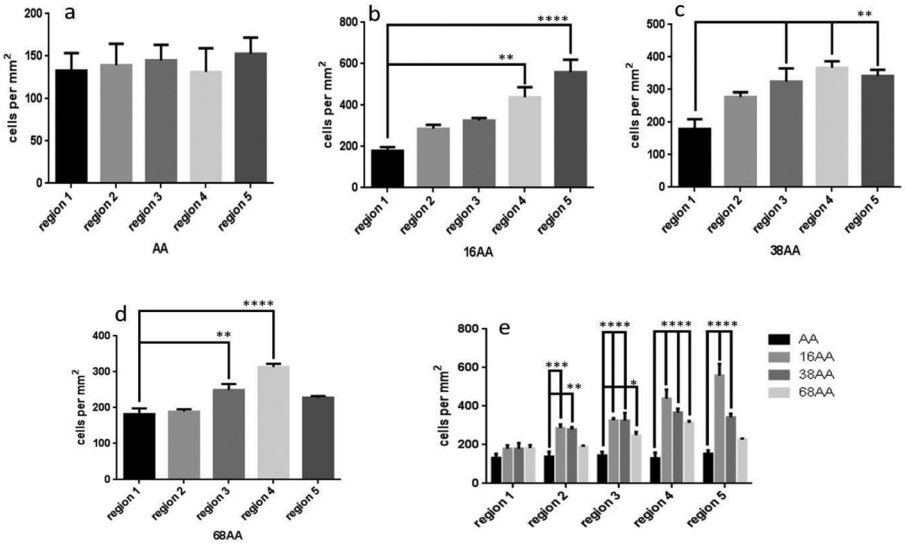

Fig. 4 Quantitative analysis of cell attachment after 12 h in culture obtained from laser scanning fluorescence microscopy images. (a) Number of cells per mm^2 across AApp coated surface, (b), (c) and (d) number of cells per mm^2 on different regions across the gradients of 16 nm, 38 nm and 68 nm AuNP with AApp overcoating. Whilst (e) shows comparison of number of cells per mm^2 between 16 nm, 38 nm and 68 nm AuNP with AApp overcoating across the different regions. * = $p < 0.05$, ** = $p < 0.01$, *** = $p < 0.001$ and **** = $p < 0.0001$. Number of experimental replicates, $n = 3$.

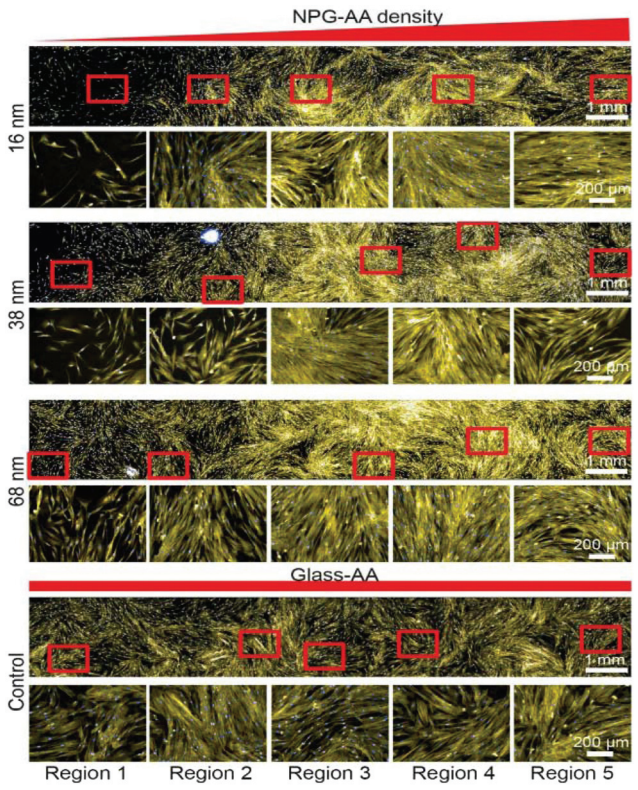

Fig. 5 Laser Scanning fluorescence microscope images across the gradients of 16 nm, 38 nm, 68 nm AuNP and the smooth AApp control showing cell proliferation after 72 h. Magnification of (20×, wide lens) was employed for capturing the images.

liferation was same across the uniformly coated AApp control. In case of 16 nm, 38 nm and 68 nm nanotopography, surface density. An increase in proliferation of cells was observed on gradients of higher nanotopography compared to gradients of smaller nanotopography.

Fig. 6 shows quantitative analysis of cell proliferation on AApp coated control and across the gradients of nanotopography. The AApp control had the same level of cell proliferation across the entire surface (Fig. 6a). As a general trend, cell proliferation increased towards greater density of nanotopography features for all gradients. In the case of nanotopography of 16 nm, the increase was statistically significant on regions 3 ($p < 0.01$), 4 ($p < 0.01$), and 5 ($p < 0.001$) relative to region 1 (Fig. 6b). The trends were similar on nanotopography of 38 nm and 68 nm where statistically significant increase in cell proliferation was seen on regions 3, 4 and 5. Interestingly, when nanotopography height was 68 nm, small drop in cell proliferation was observed in region 5 relative to region 4 (Fig. 6d), a trend consistent with the data for cell attachment (Fig. 4d). The comparative representation of cell proliferation on gradients of different nanotopography height is shown in Fig. 6e. While increased nanosize feature surface density stimulated cell proliferation on all gradients, it is evident that cells proliferated fastest on the nanotopography of greatest height.

The alkaline phosphatase (AP) activity was monitored across the gradients of nanotopography and AApp control to determine the differentiation of hDPSC into osteogenic lineages. AP was selected as a marker since is well accepted and extensively documented indicator of osteoblasts.[59] Fig. 7 shows fluorescence microscopy images of the cells stained for AP after 21 d in culture. The cells on AApp coated control showed little or no AP activity, similar to region 1 on the

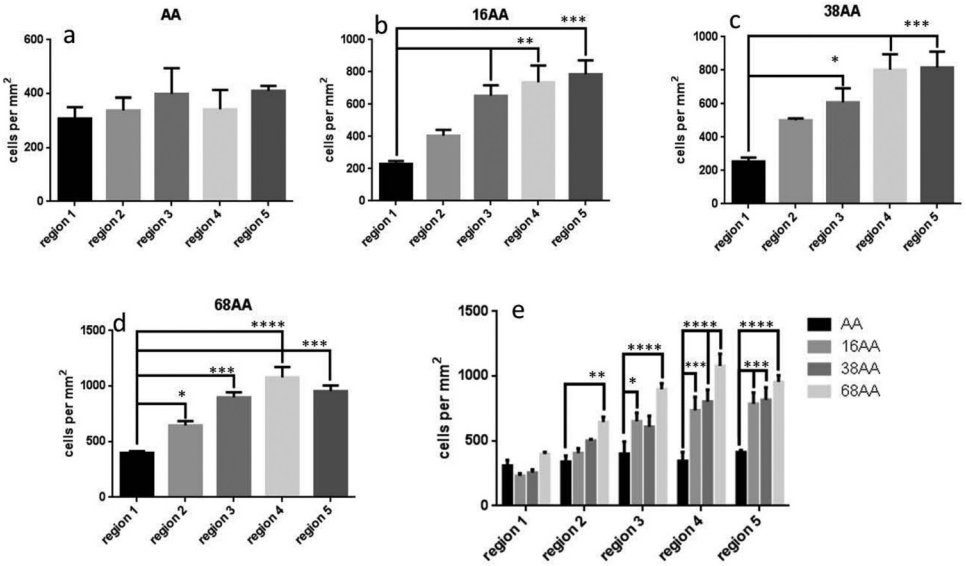

Fig. 6 Quantitative analysis of cell proliferation obtained from laser scanning fluorescence microscopy images. (a) Number of cells per mm^2 across AApp coated surface, (b), (c) and (d) number of cells per mm^2 on different regions across the gradients of 16 nm, 38 nm and 68 nm AuNP with AApp overcoating. Whilst (e) shows comparison of number of cells per mm^2 between 16 nm, 38 nm and 68 nm AuNP with AApp overcoating across different regions. * = $p < 0.05$, ** = $p < 0.01$, *** = $p < 0.001$ and **** = $p < 0.0001$. Number of experimental replicates, $n = 3$.

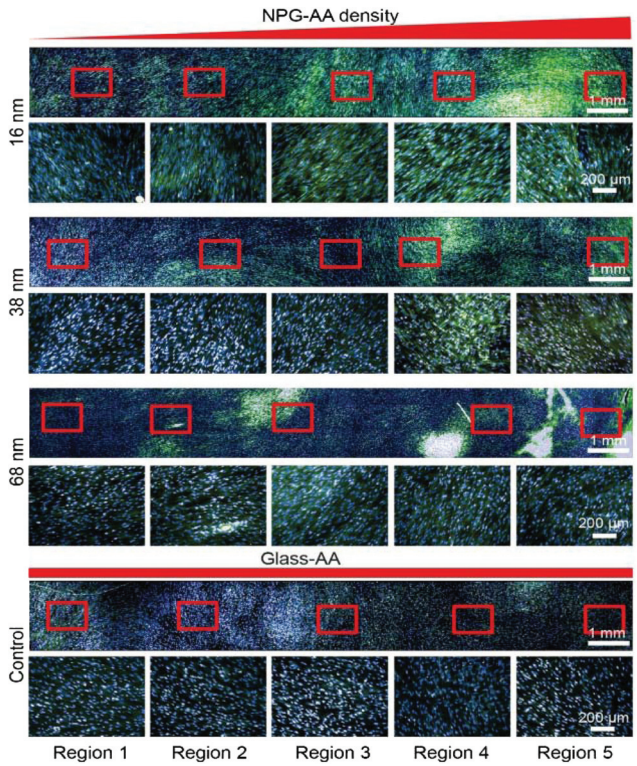

Fig. 7 Laser scanning fluorescence microscope images across the gradients of 16 nm, 38 nm, 68 nm AuNP and AApp control depicting alkaline phosphatase (AP) activity after 21 d in culture. Magnification of (20×, wide lens) was employed for capturing the images.

gradients where the nanotopography was same as on the control. This is mainly due to the lack of any surface topography and exogenous biomolecule factors on the control group. However, the images clearly show the increase in AP staining intensity (green) towards increasing density on nanoparticles. The trend was the same for all nanotopography heights but most marked on the smallest nanotopography of 16 nm.

Fig. 8 shows quantitative analysis of cell differentiation on the gradients of surface nanotopography and AApp control. The data is expressed as AP staining intensity per individual cells. Consistent with the images in Fig. 7, the levels of differentiation to osteogenic lineages was small on the smooth AApp film. When nanotopography was presented on the surface, a statistically significant trend to stronger osteogenic differentiation towards greater density of nanotopography features was observed on all gradients. In agreement with the images in Fig. 7, the smaller nanotopography of 16 nm appeared to be the strongest driver to osteogenic differentiation (Fig. 8e). The data presented in Fig. 7 and 8 demonstrate that controlled surface nanotopography is capable to promote differentiation of dental pulp stem cells (hDPSC). The cells were grown in a standard DMEM culture medium, which does not favor differentiation in particular direction.

To confirm differentiation towards osteogenic lineages, the cells were cultured in osteogenic differentiation medium (StemPro® osteogenesis differentiation kit contains components such as dexamethasone, L-glutamine, ascorbate, mesenchymal cell growth supplement and beta-glycerophosphate). Images across the nanotopography gradients and AApp control are shown in ESI Fig. S3 and S4.† The staining intensity of AP followed the same tends as reported in Fig. 7

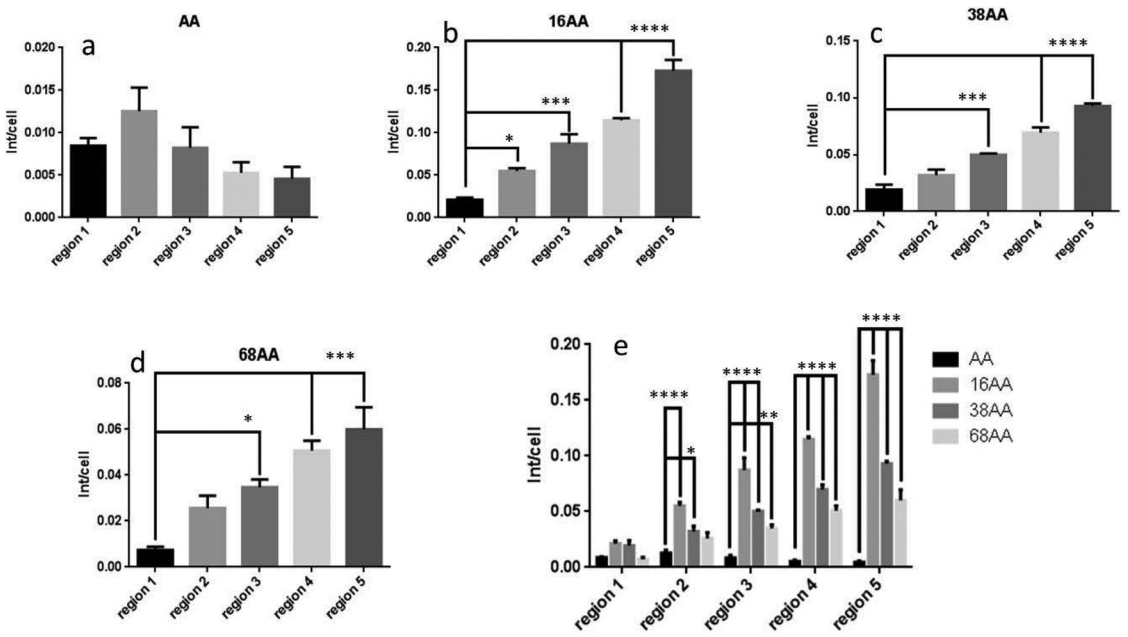

Fig. 8 Quantitative analysis of cell differentiation obtained from laser scanning fluorescence microscopy images. (a) AP intensity per cell across AApp coated surface: (b), (c) and (d) AP intensity per cell on different regions across the gradients of 16 nm, 38 nm and 68 nm AuNP. (e) Comparison of AP staining intensity per cell between different region of 16 nm, 38 nm and 68 nm nanotopography gradients. * = $p < 0.05$, ** = $p < 0.01$, *** = $p < 0.001$ and **** = $p < 0.0001$. Number of experimental replicates, $n = 3$.

and 8 above, supporting the finding of self-differentiation caused by surface nanotopography.

This study demonstrates that surface nanotopography can induce differentiation of dental pulp derived stem cells into osteoblasts without addition of any biochemical cues. Gradients of nanoparticle density were used to provide controlled surface nanotopography having engineered and characterized lateral spacing between the nanoscale features. The height of surface nanotopography was tuned by involving nanoparticles of different diamantes *i.e.* 16, 38 or 68 nm. The outermost surface chemistry was tailored by addition of a 5 nm thin amine rich layer of AApp. The gradient strategy allowed us to interrogate cellular responses with a minimum number of substrates thus avoiding errors associated with the use of multiple uniformly modified samples. Furthermore, the use of gradients speeds up analysis, reduces the number of cells used in the experiments and decreases the experimental variability by directly comparing the data obtained using the same cell population.

As a general trend, greater surface nanotopography (in terms of surface feature density) promoted cell attachment. One possible explanation could be the increase in surface area associated with greater surface nanotopography. This in turn facilitates adsorption of larger amounts of cell adhesion proteins and thus provides greater number of integrin binding sites for the cells to attach.[4] This hypothesis seems to hold well for nanotopography of 16 nm where increasing density of surface bound nanoparticles leads to greater number of attached cells. However, when the scale of nanotopography increased to 38 nm and 68 nm, despite similar or greater surface area, the number of adhered cells was smaller compared to 16 nm. Recent studies have suggested protein unfolding when attached to curved surface of nanoparticles. The phenomenon leads to exposure of hidden binding sites that may change cell adhesion dynamics.[47,60] Although, these studies were carried out with nanoparticles in solution, it is reasonable to assume that the same phenomenon occurs when nanoparticles are immobilized to solid surfaces. It may be possible that in this scenario nanoparticles of 38 nm and 68 nm lead to some degree on protein unfolding and thus present lower number of integrin binding domains relative to the increased surface area caused by nanotopography.

After two weeks in culture, the cell number was significantly greater on regions of the gradients with higher density of nanotopographical features. Larger nanoparticles of 38 nm and 68 nm promoted stronger cell proliferation. Interrogation of cell proliferation rate across the gradients, presented in Fig. S5,† revealed that in the case of nanotopography of 16 nm the increase in cell numbers towards higher nanoparticle density was merely due to the greater number of initially adhered cells. There was no statistically significant difference in the rate of cell proliferation across the 16 nm nanoparticle density gradient. However, a statistically significant increase in the rate of proliferation was seen when nanotopography increases to 38 nm and 68 nm. The data suggest that nanotopography of 68 nm is the strongest driver of cell proliferation. It should be taken into consideration that the nanotopography of 16 nm was such a strong promoter of cell attachment that space for further proliferation may not have been available to the cells. To determine the exact role of surface nano-

topography on cell proliferation rate, studies with lower seeding densities need to be carried out. However, the primary objective of this study was to determine how surface nanotopography affects the differentiation of hDPSC.

Cell differentiation was much more effective on nanotopographically modified surfaces in comparison to smooth surfaces. Differentiation towards a particular type of cell in the absence of any inducing agents points to the capacity of surface nanotopography to directly alter the fate of stem cells. Nanotopography directed differentiation of hDPSC to osteoblasts observed in our studies is consistent with what has already been reported for MSC.[30,61] Thus, taking into consideration that hDPSC are of mesenchymal phenotype, the reported results are not surprising. However, our studies allow us to examine the differentiation process as a function of both density and size of surface nanotopographical features. The evident trend associated with all three sizes of nanotopography is an increase in osteogenic differentiation with increasing surface feature density. The greater differentiation to osteoblasts towards higher nanotopography density seems to correlate with the increased number of cells shown in Fig. 3 and 4. However, while cell density reached maximum in region 4 of the gradients the differentiation increases throughout the sample. The later suggests that cell surface number and density are not sufficient to explain the phenomena that were observed. Another interesting observation points to the increase in surface area. It appears that the greater surface area on samples of 16 nm nanotopography (Fig. 1) induced the strongest alkaline phosphatase staining intensity per individual cell (Fig. 7 and 8).

The complex interplay between biological cells and biointerfaces is yet to be fully uncovered. This study and a number of others unambiguously point to the important role that surface nanotopography plays in modulating cellular responses. A large number of parameters come into play in the interactions between the surface and the cells. The attachment of proteins in terms of amount, types, orientation and unfolding are all significant in determining cell fate. Furthermore, the effect of physical cues in terms of physical and mechanical modulation of cell membrane and cytoskeleton have recently been attributed critical importance.[23,48,62] The differentiation of hDPSC to osteoblasts on rough surfaces can also be related to the natural response of these cells when needed to repair bone tissue, which is inherently rougher. The results of this study can be important in the rational design of implantable devices and tissue engineering scaffolds where the modulation of specific tissue growth is important. Furthermore, this study can instruct the design of tools and devices such as bioreactors, culture substrates and vehicles needed for the growing field of cell therapies, which are considered by many as the future of medical treatment, pointing to the possibility to control stem cell fate without the use of soluble factors such as growth factors and cytokines. The latter is important because it can make cell therapies more affordable as surface engineering is more cost effective and safer than the use soluble factors.

Experimental

Materials

Allylamine (AA) (98%, Aldrich), hydrogen tetrachloroaurate (99.9985%, ProSciTech), trisodium citrate (99%, BHD Chemicals, Australia Pty. Ltd), 2-mercaptosuccinic acid (97%, Aldrich), were used as received.

Plasma polymerization

Plasma polymerization was carried out in a custom-built reactor with a 13.56 MHz plasma generator.[63] Deposition of allylamine plasma polymer (AApp) was carried out at a pressure of 0.2 mbar for 2 min. Power used for deposition was 40 W. Using these conditions, a polymer film of thickness 23 nm was obtained. To achieve an overcoating of 5 nm, the time of deposition was 20 s. Before deposition, all substrates were cleaned by applying air plasma for 2 min at 50 W.

Synthesis of gold nanoparticles (AuNP)

AuNP were synthesized using hydrogen tetrachloroaurate (HAuCl4). Particles of 16, 38 and 68 nm diameter were synthesized by varying the amount of 1% trisodium citrate from 1 ml to 0.3 ml, respectively.[64] Surface modification of these nanoparticles was performed by using 2-mercaptosuccinic acid.[65]

Gradient formation

Allylamine coated surfaces were immersed in a solution of gold nanoparticles in a time controlled manner. The speed of immersion was controlled using Zaber T-LSR series, a computer controlled motorised linear slide using Zaber's software. For 16, 38 and 68 nm nanoparticles the speed of immersion was 10, 30 and 75 s mm^{-1} respectively. After immersion, all samples were thoroughly washed using Milli-Q water to remove the weakly bound nanoparticles.

Atomic force microscopy (AFM)

An NT-MDT NTEGRA SPM atomic force microscope (AFM) was used in non-contact mode to provide topographical images. Silicon nitride non-contact tips coated with Au on the reflective side (NT-MDT, NSG03) were used and had resonance frequencies between 65 and 100 kHz. The amplitude of oscillation was 10 nm, and the scan rate for 5 μm × 5 μm images was 0.5 Hz. All images were scaled relative to the maximum height for like-sized AuNP immobilized surfaces.

X-ray photoelectron spectroscopy

XPS analysis was used to determine the surface composition of the plasma polymer and the deposited AuNP. XPS spectra were recorded on a Specs SAGE XPS spectrometer using Al Kα radiation source ($h\nu$ = 1253.6 eV) operated at 10 kV and 20 mA. Elements present in a sample surface were identified from the survey spectrum recorded over the energy range 0–1000 eV at pass energy of 100 eV and a resolution of 0.5 eV. The areas under selected photoelectron peaks in a wide scan spectrum were used to calculate percentage atomic concentrations (excluding hydrogen). High-energy resolution (0.1 eV) spectra

were then recorded for pertinent photoelectron peaks at pass energy of 20 eV to identify the possible chemical binding environments for each element. All the binding energies (BEs) were referenced to the C 1s neutral carbon peak at 285 eV, to compensate for the effect of surface charging. The XPS analysis area was circular with a diameter of 0.7 mm. The processing and curve-fitting of the high-energy resolution spectra were performed using Casa XPS software.

Cell culture

Human dental pulp stem cells (hDPSC). Normal human impacted third molar were isolated with informed consent of patients undergoing routine extractions at the Dental Clinic of the University of Adelaide, under approved guidelines set by the University of Adelaide and Institute of Medical and Veterinary Science Human Subjects Research Committees. Tooth surfaces were cleaned using 2% chlorhexidine before cutting around the cementum–enamel junction by using sterilized discs. Then, the cracked open to reveal the pulp chamber. The pulp tissue was gently isolated then digested in a solution of 3 mg ml^{-1} collagenase type I and 4 mg ml^{-1} dispase for 1 h at 37 °C. Individual cells were obtained by passing the cells through a 70 μm strainer. Cultures were established by seeding dental pulp cells at density of 5×10^5 into T-75 flasks in culture media, (DMEM supplemented with 10% fetal bovine serum, 2 mM glutaMAX, 100 IU mL^{-1} penicillin, and 100 μg ml^{-1} streptomycin) (all from Life Technologies), then incubated at 37 °C in 5% CO_2 for 1 week. The cell culture medium was changed to remove non-adherent cells 12 h after cell seeding. The cells were collected and analyzed for minimal criteria to define human mesenchymal stem cells.[15] Briefly, primary hDPSCs were fixed in 4% formalin for 20 min. Cells were treated with blocking solution of 10% serum from the species in which the secondary antibody was raised for 30 min to block non-specific binding of the primary antibodies. The cells reacted with primary antibodies diluted in dPBS for 16 h at 4 °C. Antibodies anti-CD14, anti-CD34, anti-CD45, anti-COL II was used as a negative marker and anti-CD44, anti-VCAM-1, anti-COL III, anti-COL I, and anti-FGF-2 was used as positive marker. Secondary antibodies conjugated with FITC or PE was used to detect the primary antibodies.

HDPSC attachment to gradient surfaces. Prior to incubation of hDPSC on the gradients of 16, 38 and 68 nm monodispersed AuNP with a homogeneous overcoating of AApp on these surfaces, the AuNP gradient coverslip glasses were washed with copious amounts of sterile Dulbecco's phosphate-buffered saline solution (PBS) (Sigma) to remove any excess residuals. Then, the coverslips were sterilized with 400 U ml^{-1} penicillin, 400 mg ml^{-1} streptomycin, and 500 ng ml^{-1} amphotericin B (Life Technologies) in sterile PBS for 1 h then were washed three times in sterile PBS. Coverslip samples containing the AuNP gradients with a homogeneous overcoating of AApp were placed in 24-well plates (Nunc) and seeded with hDPSC at a density of 5×10^4 cells per ml per well in fresh cell culture medium. As controls, cells were also plated onto sterile round 13 mm AApp coated glass coverslips ($n = 3$) at the same density.

Cell adhesion and proliferation. Cells were seeded onto the surface of sterilized 16, 38 and 68 nm AuNP gradients with a homogeneous overcoating of AApp at a cell density of 5×10^4 cells per ml per well. Sterile round 13 mm AApp coated glass coverslips were used as control. Cells were incubated for 12 and 72 h at 37 °C with 5% CO_2, in a humidified incubator. After the incubation time, the cells were gently rinsed with PBS to remove unattached cells. Then cultured cells were fixed with 4% paraformaldehyde solution (Electron Microscopy Science) for 10 min. The samples were rinsed again in PBS and then were incubated in 0.1% Triton X-100 in PBS at room temperature for 5 min, then rinsed with PBS. Nuclei of cells were stained with 2 μg ml^{-1} Hoechst 33342 (Life Technologies) for 10 min at room temperature. Actin was stained with 100 μM TRITC-labelled Phalloidin (Sigma-Aldrich) for 1 h. hDPSC attachment and proliferation were monitored by full automated high content screening microscopy (Operetta, PerkinElmer). Gradients were divided into five equally broad regions of increasing AuNP density (regions from low density of AuNP of the gradient: 0.5–2.9 mm = region 1, 2.9–5.3 mm = region 2, 5.3–7.7 mm = region 3, 7.7–10.1 mm = region 4, and finally 10.1–12.5 mm = region 5). The cell density was evaluated by counting the number of attached cells at five different regions for each region on the gradient surfaces for the 3 days of culture. Cell attachment and cell proliferation experiments were repeated three times on independent samples.

Osteogenic differentiation assay. The differentiation of hDPSC into the osteo lineage was assessed *via* immunofluorescence technique detecting the alkaline phosphatase (ALP) activity. The cells were incubated on 16, 38 and 68 nm AuNP gradients with a homogeneous overcoating of AApp and round 13 mm AApp coated glass coverslips (control) at density of 5×10^4 cells per ml for 24 h in low-glucose DMEM containing 10% FBS. Afterwards, medium was replaced by osteogenic medium (StemPro® osteogenesis differentiation kit). hDPSC were cultivated up to 21 d under differentiation conditions, while medium was changed every three days. To investigate the effects of the AuNP gradient on hDPSC behavior (in separate experiment), no other bioactive factors were added to the culture medium (low-glucose DMEM supplemented with 15% fetal bovine serum, 2 mM glutaMAX, 100 IU ml^{-1} penicillin, and 100 μg ml^{-1} streptomycin). Feeding was performed every three days with fresh low-glucose DMEM medium consisting in 15% fetal bovine serum, 2 mM glutaMAX, 100 IU ml^{-1} penicillin, and 100 μg ml^{-1} streptomycin. ALP activity was applied after 21 d of differentiation. In order to stain for ALP, cultured cells were gently rinsed with PBS and fixed in 4% paraformaldehyde solution for 10 min at room temperature. To allow the primary antibodies to enter the cells, the samples were rinsed again in PBS and then incubated in 0.25% Triton X-100 in PBS at room temperature for 5 min, then blocked with 10% serum (in PBS) from the species that the secondary antibody (donkey) was raised in for 1 h at room temperature. Immunofluorescence was performed by incubating the cells with rabbit anti ALP monoclonal IgG (ALP, Santa Cruz, diluted 1 : 200 in PBS) as a osteo lineage marker. After incubation with

the primary antibodies for overnight at 4 °C and washing three times with PBS, the secondary antibody, FITC-conjugated donkey anti rabbit (Santa Cruz, diluted 1 : 100 in PBS) was added for 1 h at room temperature. Negative controls were carried out by eliminating the primary antibody labelling step from the procedure, which in all cases resulted in a complete loss of signal from fluorescence-labelled secondary antibodies. Finally, the nuclei were counterstained with 2 μg ml^{-1} Hoechst 33342 in PBS for 10 min, rinsed with PBS. Gradients were divided into five equal regions of gradually increasing AuNP as previously described, and cell behavior was compared between each zone. Images were obtained on a full automated inverted fluorescence microscope (Operetta) equipped with Harmony imaging and analysing software. Immunofluorescence analysis was repeated in three independent experiments.

Conclusions

This study reveals the role of surface nanotopography on the attachment, proliferation and differentiation of hDPSC. We designed and utilized gradients of nanotopography generated from three different sized gold nanoparticles (*i.e.* 16, 38 and 68 nm) which had uniformly tailored outermost surface chemistry of plasma polymerised allylamine. hDPSC adhered in greater numbers and proliferated faster on the regions of the gradients with higher density of nanotopography features. Nanoparticles diameters of 16 nm were most effective in enhancing cell attachment with those of 38 nm and 68 nm showing greater proliferation rates. Moreover, we found that greater surface nanotopography density directed the differentiation of hDPSC to osteogenic lineages and the 16 nm sized nanotopography being the strongest driver. In addition to being the first work to explore the effect of surface roughness on hDPSC, this study demonstrates that carefully tuned surface nanotopography can be used to manipulate and guide the proliferation and differentiation of these cells. The outcomes of this study can be important in the rational design of the next generation of biomedical devices and tissue engineering constructs where control over the growth of different tissues is required. These results are also important for the growing field of cell therapies where control of stem cell fate is an essential requirement.

Conflicts of interest

There are no conflicts to declare.

Acknowledgements

KV thanks ARC (DP15104212) and NHMRC Fellowship (APP1122825) and NV thanks NHMRC (APP595901) for their support.

References

1 F. Variola, J. B. Brunski, G. Orsini, P. T. de Oliveira, R. Wazen and A. Nanci, *Nanoscale*, 2011, **3**, 335.
2 L. Tang, P. Thevenot and W. Hu, *Curr. Top. Med. Chem.*, 2008, **8**, 270.
3 M. S. Castro Raucci, M. S. Francischini, L. N. Teixeira, E. P. Ferraz, H. B. Lopes, P. T. de Oliveira, M. Q. Hassan, A. L. Losa and M. M. Beloti, *J. Cell. Biochem.*, 2016, **7**, 1718.
4 M. J. P. Biggs, R. G. Richards and M. J. Dalby, *Nanomed. Nanotechnol.*, 2010, **6**, 619.
5 S. Brody, T. Anilkumar, S. Liliensiek, J. A. Last, C. J. Murphy and A. Pandit, *Tissue Eng.*, 2006, **12**, 413.
6 S. J. Liliensiek, J. A. Wood, J. Yong, R. Auerbach, P. F. Nealey and C. J. Murphy, *Biomaterials*, 2010, **31**, 5418.
7 C. N. Elias and L. Meirelles, *Expert Rev. Med. Devices*, 2010, **7**, 241.
8 E. Bressan, L. Sbricoli, R. Guazzo, I. Tocco, M. Roman, V. Vindigni, E. Stellini, C. Gardin, L. Ferroni and S. Sivolella, *Int. J. Mol. Sci.*, 2013, **14**, 1918.
9 M. J. Dalby, N. Gadegaard, R. Tare, A. Andar, M. O. Riehle, P. Herzyk, C. D. W. Wilkinson and R. O. C. Oreffo, *Nat. Mater.*, 2007, **6**, 997.
10 A. Klymov, L. Prodanov, E. Lamers, J. A. Jansen and X. F. Walboomers, *Biomater. Sci.*, 2013, **1**, 135.
11 P. Decuzzi and M. Ferrari, *Biomaterials*, 2010, **31**, 173.
12 K. Sakai, A. Yamamoto, K. Matsubara, S. Nakamura, M. Naruse, M. Yamagata, K. Sakamoto, R. Tauchi, N. Wakao and S. Imagama, *J. Clin. Invest.*, 2012, **122**, 80.
13 P. D. Potdar and Y. D. Jethmalani, *World J. Stem Cells*, 2015, **7**, 839.
14 M. Tatullo, M. Marrelli, K. M. Shakesheff and L. J. White, *J. Tissue Eng. Regener. Med.*, 2015, **9**, 1205.
15 S. Gronthos, M. Mankani, J. Brahim, P. G. Robey and S. Shi, *Proc. Natl. Acad. Sci. U. S. A.*, 2000, **97**, 13625.
16 X. Yan, H. Qin, C. Qu, R. S. Tuan, S. Shi and G. T.-J. Huang, *Stem Cells Dev.*, 2010, **19**, 469.
17 N. Tamaoki, K. Takahashi, T. Tanaka, T. Ichisaka, 860652H. Aoki, T. Takeda-Kawaguchi, K. Iida, T. Kunisada, T. Shibata, S. Yamanaka and K. Tezuka, *J. Dent. Res.*, 2010, **89**, 773.
18 B. C. Kim, H. Bae, I. K. Kwon, E. J. Lee, J. H. Park, A. Khademhosseini and Y. S. Hwang, *Tissue Eng., Part B*, 2012, **18**, 235.
19 C. Gandia, A. Arminan, J. M. García-Verdugo, E. Lledo, A. Ruiz, M. D. Minana, J. Sanchez-Torrijos, R. Paya, V. Mirabet and F. Carbonell-Uberos, *Stem Cells*, 2008, **26**, 638.
20 R. Patil, B. M. Kumar, W. J. Lee, R. H. Jeon, S. J. Jang, Y. M. Lee, B. W. Park, J. H. Byun, C. S. Ahn, J. W. Kim and G. J. Rho, *Exp. Cell Res.*, 2014, **320**, 92.
21 N. F. Lizier, A. Kerkis, C. M. Gomes, J. Hebling, C. F. Oliveira, A. I. Caplan and I. Kerkis, *PLoS One*, 2012, **7**, e39885.

22 M. P. Lutolf, P. M. Gilbert and H. M. Blau, *Nature*, 2009, **462**, 433.
23 S. R. Ghaemi, F. J. Harding, B. Delalat, S. Gronthos and N. H. Voelcker, *Biomaterials*, 2013, **34**, 7601.
24 D. Woodbury, E. J. Schwarz, D. J. Prockop and I. B. Black, *J. Neurosci. Res.*, 2000, **61**, 364.
25 L. Qian and W. M. Saltzman, *Biomaterials*, 2004, **25**, 1331.
26 B. Delalat, A. Mierczynska, S. R. Ghaemi, A. Cavallaro, F. J. Harding, K. Vasilev and N. H. Voelcker, *Adv. Funct. Mater.*, 2015, **25**, 2737.
27 X. Liu, Q. Feng, A. Bachhuka and K. Vasilev, *ACS Appl. Mater. Interfaces*, 2014, **6**, 9733.
28 F. Harding, R. Goreham, R. Short, K. Vasilev and N. H. Voelcker, *Adv. Healthcare Mater.*, 2013, **2**, 585.
29 R. J. McMurray, N. Gadegaard, P. M. Tsimbouri, K. V. Burgess, L. E. McNamara, R. Tare, K. Murawski, E. Kingham, R. O. Oreffo and M. J. Dalby, *Nat. Mater.*, 2011, **10**, 637.
30 M. J. Dalby, N. Gadegaard and R. O. Oreffo, *Nat. Mater.*, 2014, **13**, 558.
31 E. K. Yim and K. W. Leong, *Nanomed. Nanotechnol. Biol. Med.*, 2005, **1**, 10.
32 V. Vogel and M. P. Sheetz, *Curr. Opin. Cell Biol.*, 2009, **21**, 38.
33 A. Bachhuka, J. Hayball, L. E. Smith and K. Vasilev, *ACS Appl. Mater. Sci.*, 2015, **7**, 23767.
34 S. N. Christo, A. Bachhuka, K. R. Diener, A. Mierczynska, J. D. Hayball and K. Vasilev, *Adv. Healthcare Mater.*, 2016, **8**, 956.
35 Y. Khung, G. Barritt and N. Voelcker, *Exp. Cell Res.*, 2008, **314**, 789.
36 M. J. Dalby, D. McCloy, M. Robertson, H. Agheli, D. Sutherland, S. Affrossman and R. O. Oreffo, *Biomaterials*, 2006, **27**, 2980.
37 A. S. Curtis and C. D. Wilkinson, *J. Biomater. Sci., Polym. Ed.*, 1998, **9**, 1313.
38 J.-Y. Jang, S. W. Lee, S. H. Park, J. W. Shin, C. Mun, S.-H. Kim, D. H. Kim and J.-W. Shin, *BioMed. Res. Int.*, 2011, 860652.
39 K. S. Brammer, C. Choi, C. J. Frandsen, S. Oh and S. Jin, *Acta Biomater.*, 2011, **7**, 683.
40 L. R. Clements, P.-Y. Wang, W.-B. Tsai, H. Thissen and N. H. Voelcker, *Lab Chip*, 2012, **12**, 1480.
41 P. Y. Wang, L. R. Clements, H. Thissen, A. Jane, W. B. Tsai and N. H. Voelcker, *Adv. Funct. Mater.*, 2012, **22**, 3414.
42 P.-Y. Wang, L. R. Clements, H. Thissen, S.-C. Hung, N.-C. Cheng, W.-B. Tsai and N. H. Voelcker, *RSC Adv.*, 2012, **2**, 12857.
43 P.-Y. Wang, L. R. Clements, H. Thissen, W.-B. Tsai and N. H. Voelcker, *Biomater. Sci.*, 2013, **1**, 924.
44 C. J. Wilson, R. E. Clegg, D. I. Leavesley and M. J. Pearcy, *Tissue Eng.*, 2005, **11**, 1.
45 F. Guilak, D. M. Cohen, B. T. Estes, J. M. Gimble, W. Liedtke and C. S. Chen, *Cell Stem Cell*, 2009, **5**, 17.
46 Z. J. Deng, M. Liang, M. Monteiro, I. Toth and R. F. Minchin, *Nat. Nanotechnol.*, 2011, **6**, 39.
47 Z. J. Deng, M. Liang, I. Toth, M. J. Monteiro and R. F. Minchin, *ACS Nano*, 2012, **6**, 8962.
48 M. Schernthaner, B. Reisinger, H. Wolinski, S. D. Kohlwein, A. Trantina-Yates, M. Fahrner, C. Romanin, H. Itani, D. Stifter and G. Leitinger, *Acta Biomater.*, 2012, **8**, 2953.
49 T. P. Kunzler, T. Drobek, M. Schuler and N. D. Spencer, *Biomater.*, 2007, **28**, 2175.
50 E. K. Yim, E. M. Darling, K. Kulangara, F. Guilak and K. W. Leong, *Biomater.*, 2010, **31**, 1299.
51 R. Ravichandran, S. Liao, C. C. Ng, C. K. Chan, M. Raghunath and S. Ramakrishna, *World J. Stem Cells*, 2009, **1**, 55.
52 R. V. Goreham, A. Mierczynska, L. E. Smith, R. Sedev and K. Vasilev, *RSC Adv.*, 2013, **3**, 10309.
53 M. Ramiasa-MacGregor, A. Mierczynska, R. Sedev and K. Vasilev, *Nanoscale*, 2016, **8**, 4635.
54 A. Mierczynska, A. Michelmore, A. Tripathi, R. V. Goreham, R. Sedev and K. Vasilev, *Soft Matter*, 2012, **8**, 8399.
55 J. C. Ruiz, S. Taheri, A. Michelmore, D. E. Robinson, R. D. Short, K. Vasilev and R. Förch, *Plasma Processes Polym.*, 2014, **11**, 888.
56 R. V. Goreham, A. Mierczynska, M. Pierce, R. D. Short, S. Taheri, A. Bachhuka, A. Cavallaro, L. E. Smith and K. Vasilev, *Thin Solid Films*, 2013, **528**, 106.
57 K. Vasilev, A. Michelmore, P. Martinek, J. Chan, V. Sah, H. J. Griesser and R. D. Short, *Plasma Processes Polym.*, 2010, **7**, 824.
58 Z. Bo, Y. Tian, Z. J. Han, S. Wu, S. Zhang, J. Yan, K. Cen and K. K. Ostrikov, *Nanoscale Horiz.*, 2017, **2**(2), 89–98.
59 M. Elsafadi, M. Manikandan, M. Atteya, J. A. Hashmi, Z. Iqbal, A. Aldahmash, M. Alfayez, M. Kassem and A. Mahmood, *Stem Cells Int.*, 2016, **2016**, 9378081.
60 Z. J. Deng, M. T. Liang, M. Monteiro, I. Toth and R. F. Minchin, *Nat. Nanotechnol.*, 2011, **6**, 39.
61 S. Oh, K. S. Brammer, Y. J. Li, D. Teng, A. J. Engler, S. Chien and S. Jin, *Proc.Natl. Acad. Sci. U. S. A.*, 2009, **106**, 2130.
62 O. Mashinchian, L.-A. Turner, M. J. Dalby, S. Laurent, M. A. Shokrgozar, S. Bonakdar, M. Imani and M. Mahmoudi, *Nanomed.*, 2015, **10**, 829.
63 K. Vasilev, A. Michelmore, P. Martinek, J. Chan, V. Sah, H. J. Griesser and R. D. Short, *Plasma Processes Polym.*, 2010, **7**, 824.
64 R. V. Goreham, R. D. Short and K. Vasilev, *J. Phys. Chem. C*, 2011, **115**, 3429.
65 T. Zhu, K. Vasilev, M. Kreiter, S. Mittler and W. Knoll, *Langmuir*, 2003, **19**, 9518.